

Experimental demonstration of an inertial collimation mechanism in nested outflows

R. Yurchak,¹ A. Ravasio,^{1,*} A. Pelka,¹ S. Pikuz Jr.,² E. Falize,³ T. Vinci,¹ M. Koenig,¹ B. Loupias,³ A. Benuzzi-Mounaix,¹ M. Fatenejad,⁴ P. Tzeferacos,⁴ D. Q. Lamb,⁴ and E.G. Blackman⁵

¹*LULI, Ecole Polytechnique, CNRS, CEA, UPMC, Route de Saclay, 91128 Palaiseau, France*

²*Joint Institute for High Temperatures RAS, 13-2 Izorskaya st., Moscow, 125412 Russia.*

³*CEA-DAM-DIF, F-91297 Arpajon, France*

⁴*Flash Center for Computational Science, University of Chicago, IL 60637*

⁵*Department of Physics and Astronomy, University of Rochester, Rochester, NY 14627, USA*

(Dated: March 20, 2014)

Interaction between a central outflow and a surrounding wind is common in astrophysical sources powered by accretion. Understanding how the interaction might help to collimate the inner central outflow is of interest for assessing astrophysical jet formation paradigms. In this context, we studied the interaction between two nested supersonic plasma flows generated by focusing a long pulse high-energy laser beam onto a solid target. A nested geometry was created by shaping the energy distribution at the focal spot with a dedicated phase plate. Optical and X-ray diagnostics were used to study the interacting flows. Experimental results and numerical hydrodynamic simulations indeed show the formation of strongly collimated jets. Our work experimentally confirms the “shock-focused inertial confinement” mechanism proposed in previous theoretical astrophysics investigations.

PACS numbers: 64.30.+t, 52.35.Tc, 62.50.+p, 52.50.Lp

Introduction-Supersonic jets are common in astrophysics, emanate from such sources as newly forming young stellar objects (YSOs) [1], active galactic nuclei (AGN) [2, 3], planetary and pre-planetary nebulae (PPN and PPN) [4] and micro-quasars [5]. Their sustained collimation over large distances is not yet completely understood. Both magnetohydrodynamic (MHD) and hydrodynamic (HD) processes may be important. Often the jets propagate within a surrounding wind or envelope, as observed in YSOs [6], AGN [7], and in PN, where fast collimated winds sweep into a slower denser wind ejected most strongly during the PPN phase [8, 9]. For YSOs and AGN a direct connection between disks and jets has been established and there is emerging consensus for such in the PPN/PN context as well [10–12]. The question of how different time-dependent ambient thermal and ram pressures affect jet collimation arises quite generally [13–17].

The role of the ambient medium can be important even if the inner outflows are magnetically driven [18, 19]. Recent 3D MHD simulations of laser driven plasma experiments have looked at the possible magnetic field collimation of wide-angle winds into HD jets [20] and interpreted this as analogous to hydrodynamic collimation of an inner flow by a torus. Astrophysical jet launch regions are generally not observationally resolved, being obscured by high opacities. It is therefore valuable to distill the distinct physics of MHD and HD effects via alternative methods.

Combined with numerical simulations and theory, experiments bring new contributions to the subject. Some jet propagation and collimation mechanisms within steady ambient backgrounds have been studied experimentally [21–23]. Crosswinds were also used to study jet

deflection and C-shape structures [24]. Here we present results from a new experimental approach aimed at investigating the time dependent HD collimation of an inner isotropically supersonic expanding plasma by a surrounding time-evolving supersonic ambient flow.

Experimental Setup-The experiment was performed on the LULI2000 laser facility at the LULI Laboratory, in France. The set-up is shown schematically in Fig. 1. A long pulse ($\tau_L \sim 1.5$ ns) high-energy ($E_L \sim 400$ J at $\lambda_L = 527$ nm) laser beam was used to produce supersonic plasma flows via interaction with solid targets. To create the nested configuration, we have designed a phase plate able to generate a laser energy distribution with a (100 μm) central circular spot and a thinner (75 μm) outer ring. Targets manufactured to match this pattern were made of a central iron disk (15 μm thick Fe) and a peripheral plastic ring (CH, also 15 μm thick), sitting on a CHAl pusher. Upon laser impact, a shock wave is launched in the pusher and transmitted to the Fe and CH layers. Once this shock reaches the rear side of the target, supersonic plasmas are formed from the outer plastic ring and from the central iron disk.

To probe the interacting flows, we used rear-side and transverse optical diagnostics, in addition to transverse X-ray radiography. Optical probes were applied to the low density CH plasma and X-rays were used to characterize the inner iron flow which is opaque to optical radiation. Transverse optical diagnostics included time-resolved self-emission, shadowgraphy and interferometry, while time-resolved 1D self-emission and 2D self-emission snapshots were implemented at the rear side of the target. This ensemble allowed us to measure the plastic flow velocity, morphology and electron density.

Results- Typical data showing time resolved 1-D self-

emission are shown in Fig. 2. In Fig. 2a, the ring part of the laser spot was blocked and the data show a typical plasma release, with the iron expanding and cooling into vacuum. Fig. 2b shows the case of a complete target, with the plastic ring added. Since the plastic is transparent to visible light, we can follow the shock front in the plastic layer, and measure the shock velocity D . Typical D values are ~ 30 km/s. When the shock breaks out, the CH unloads into vacuum at ~ 70 km/s, as measured from the transverse time-resolved self-emission. The shock wave propagates more slowly in iron than plastic because of different impedances. Therefore the Fe flow unloads into vacuum after the CH and then swiftly collides with the radially expanding CH. Bright emission is observed from this collision and it is associated to a shock generation, as we will discuss below. The time evolution of the collision emission shows that the iron is confined by the surrounding CH flow. Later, the CH flows themselves collapse on axis, generating highly collimated emission.

X-ray radiography confirms the iron collimation by the plastic flows (Fig. 3). The X-ray source was generated by driving a copper back-lighter with the short pulse beam (~ 1 ps) of the pico2000 laser system. The incident X-ray spectrum accounted for intense K- α emission line at ~ 8 keV, superimposed on a weaker bremsstrahlung continuum. At these X-ray energies, the outer plastic plasma is nearly transparent, while the iron flow is highly absorbing. The central (iron) jet morphology can therefore be identified without being disturbed by the surrounding flow. Again we have compared shots taken with and without the surrounding plastic. Typical results are presented in figure 3a and 3e for a probing delay of 35 ns. As in Fig. 2a, the case of iron alone (Fig. 3a) exhibits quasi-spherical adiabatic expansion. As soon as the plastic flow is added, the expansion is strongly reduced and the flow is collimated. Fig. 3e thus confirms what the optical data suggested more indirectly. By varying the delay of the back-lighter to the main beam from 8 ns to 100 ns, we monitored the time evolution of the iron flow. The results are presented in Fig. 3b-h, confirming the emergence of a thin jet from an initially uncollimated plasma.

Overall, the data of Fig. 3 reveal different phases of jet evolution. First, the iron expands. A high density layer is formed at the interface between the iron and plastic plasma, detected as a reduced transmission at the Fe boundary in the radiographs of figure 3c. The plasma flow is subsequently focused on the axis, with a convergence point clearly observable at 35 ns (Fig. 3e). At longer times, a narrow collimated feature is observed remaining stable for 80 ns (figure 3g).

The jet longitudinal extension (i.e. along the propagation axis) linearly increases from a few $100 \mu\text{m}$ at earlier times (Fig. 3b-e) to mm scales at later times (Fig. 3f-g). Its radius shrinks in time and can be fit by the expression $r(\mu\text{m}) \sim 56 \cdot e^{-t(\text{ns})/13} + 53$. The iron confinement sustains high surface densities. From transmission data we mea-

sure $100 \text{ g} \cdot \text{cm}^{-3} \cdot \mu\text{m}$ at earlier times (8 ns) and $12 \text{ g} \cdot \text{cm}^{-3} \cdot \mu\text{m}$ at 80 ns. The corresponding densities at the mid length of the jet are obtained by Abel inversion resulting in 0.6 g/cc and 0.1 g/cc respectively. At these densities, typical aspect ratios (AR, length-to-width) up to ~ 5 are obtained.

Numerical Simulations and Physical Interpretation- Using the FLASH multi-physics AMR (Adaptive Mesh Refinement) code [25] (recently extended to include high energy density physics capabilities [26]), we have simulated the interaction of the iron in with the surrounding plastic in 2-D. We used the un-split 3-temperature HD solver with the energy deposition module and a radiation transfer modeled by multi-group diffusion with 32 groups. Iron and plastic shock breakout times measured by the rear-side self-emission diagnostics, are used to calibrate the laser intensity in the simulations. The reliability of the simulations up to 55 ns is also verified by interferometry and shadowgraphy data. At later times, the cumulative incertitude associated with equations of state, opacities, conduction models, species mixing, etc, limits the accuracy of the numerical results. Detailed modeling of the plasma parameters is beyond the present scope, but the present simulations do very much help to convey the global flow dynamics and physical processes

Fig. 4a shows density and pressure maps at different times, with the corresponding synthetic radiographs (Fig. 4b-f). These panels can be directly compared to the experimental results. Generally, there is substantial agreement with the data shown in Fig. 3b-h with respect to the presence and time evolution of the iron jet. All of the different evolutionary phases are seen in the simulations: confinement; focusing with a convergence point (Fig. 4c-d); and long lasting collimation (Fig. 4e-f). Simulations also show that the iron collimation initiates at a shock wave from the collision between supersonic CH and Fe plasmas. Signatures of the shock are seen in the simulated density and pressure maps, which indicate three density discontinuities and two pressure jumps, corresponding to the inner and outer density features (Fig. 5). These features correspond to a transmitted shock in Fe, a reflected shock in CH and a contact discontinuity between them. The shock is also seen in the simulated X-ray radiographs as a stronger absorption layer and corresponds to the high density shocked iron, already observed in the experimental data. Together with the increase in the emitted radiation recorded at the iron/plastic boundary from the rear side self-emission, the experimental measurements are consistent with the picture revealed by simulations.

The presence of the shock and its shape reveals the dynamics and collimation of the iron flow. The shock shape is determined by the relative expansion of the CH and Fe plasmas. In our case, a converging conical shock is generated in Fe, since the CH plasma forms earlier and expands farther than the Fe. As the Fe expands and strikes

the shock surface obliquely, only the normal component of the post-shock velocity is reduced, so the shock marks the locus at which the Fe flow vector focuses toward the axis. (Fig. 5). This mechanism was previously identified analytically in astrophysical studies [27] and later in HD simulations [13, 14, 28]. It is called “shock-focused inertial confinement” (SFIC) and may help collimate flows from Young Stellar Objects (YSO) and PN, particularly when cooling is added [29]. Our results give the first experimental confirmation of this scenario, without cooling.

Astrophysical Relevance- The importance of the experiment is bolstered when experimental parameters correspond to those of specific astrophysical systems [30]. The characteristic experimental parameters for the iron flow are shown in the first column of table I. They indicate a highly collimated ($AR \sim 5$), supersonic flow ($M \sim 10$) in a pure HD regime where radiative ($\chi \gg 1$) and microphysical conductive ($Pe \gg 1$) effects are negligible. Table I also shows representative parameter regimes for YSOs [1, 6, 31], AGN [2, 7], and PPN [4, 8, 9, 11, 12], near the inner collimation scales of these jets. Note that $Pe \gg 1$ in all cases so that microphysics of thermal conduction does not affect the bulk dynamics. YSOs are the most similar to the experiments, except for their cooling.

For PPN, the young jets of low density seem to interact with the denser wind of the post-AGB star [12], resulting in a density ratio < 1 . AGN jets are also of lower density than their surrounding wide angle winds and they are relativistic, differing in those respects from the experiments. Nevertheless, jet collimation in the experiment arises because the momentum of the outer outflow can redirect that of the inner outflow, and this requirement would be the same regardless of the density ratio of whether the flows are relativistic. So the nested wind structure and basic principles of inertial collimation still apply to PPN and AGN, but the specific predictions for shock location and geometry could be different.

Conclusions- Motivated by astrophysical contexts where jets are associated with accretion engines, we have established an experimental platform to study the collimating interaction between high Mach outflows. We have experimentally confirmed the efficacy of inertial mechanisms in producing highly collimated outflows in an HD regime, similar to jets from YSOs, but also relevant for systems such as AGN and PPN. Most importantly, we have experimentally verified the SFIC mechanism suggested in previous astrophysical studies, exemplifying the contribution that such laboratory experiments can bring to the enterprise of astrophysics. Further insights on the jet collimation paradigm can be accessed by combining inertial with magnetic and radiative effects in future experiments.

Acknowledgments- We gratefully acknowledge support of the technical staff at the LULI 2000 laser facility and H. Nakatsutsumi for target fabrication. The FLASH code

was developed in part by the U.S. DOE and NSF-funded Flash Center for Computational Science at the Univ. of Chicago. This work was performed using HPC resources from GENCI-IDRIS (Grant 2013-i2013057066). EB acknowledges NSF grant AST-1109285.

* alessandra.ravasio@polytechnique.fr

- [1] B. Reipurth, J. Bally, ARA&A, 39, **403** (2001)
- [2] A. Ferrari, ARA&A **36** 539 (1998).
- [3] A.P. Marscher AIP Conf. Proc. **856**, 1 (2006).
- [4] B. Balick, A. Frank, ARA&A **40**, 439 (2002).
- [5] I.F. Mirabel, L.F. Rodríguez ARA&A, 37, **409**(1999).
- [6] H. Arce, A.A. Goodman, ApJ, 575, **928** (2002).
- [7] F. Tombesi *et al.* Mon. Not. R. Astron. Soc, **424**, 754 (2012).
- [8] V. Bujarrabal, A. Castro-Carrizo, J. Alcolea, C. Sánchez Contreras, A&A, 377, **868** (2001)
- [9] J.R. Rizzo *et al.* A&A, 560, **A82** (2013)
- [10] N. Soker, ApJ, 496, **833** (1998)
- [11] E.G. Blackman, S. Lucchini, in press MNRAS, arXiv:1312.5372 (2014)
- [12] A.N. Witt *et al.* ApJ, 693, **1946** (2009)
- [13] V. Icke, G. Mellema, B. Balick, F. Eulderink, A. Frank, Nature, 355 **524**, (1993)
- [14] A. Frank, A. Noriega-Crespo, Astron. Astrophys. **290**, 643 (1994).
- [15] A. Frank *et al.* Astrophys. J. **471**, **L53** (1996).
- [16] E.G. Blackman, R. Perna, , Astrophys. J. **601**, L71 (2004).
- [17] T.J. Dennis *et al.*, Astrophys. J. **707**, 1485 (2009).
- [18] C. Fendt, Astrophys. J. , **692**, 346 (2009)
- [19] D. Lynden-Bell, MNRAS, 341, **1360** (2003).
- [20] A. Ciardi *et al.*, Phys. Rev. Lett. **110**, 025002 (2013).
- [21] S.V. Lebedev *et al.*, Astrophys. J. **564**, 113 (2002).
- [22] B. Loupiaz *et al.*, Phys. Rev. Lett. **99**, 265001 (2007).
- [23] D.R. Farley *et al.*, Phys. Rev. Lett. **83**, 1982 (1999).
- [24] S.V. Lebedev *et al.*, Astrophys. J. **616**, 988 (2004).
- [25] B. Fryxell, *et al.*, Astrophys. J. **131**, 273 (2000).
- [26] C. Orban, *et al.* eprint arXiv:1306.1584 (2013).
- [27] R.H. Sanders, , Astrophys. J. **266**, 73 (1983).
- [28] A. Frank, G. Mellema Astrophys. J. **472**, 684 (1996).
- [29] G. Mellema, A. Frank, Mon. Not. R. Astr. Soc. **292**, 795 (1997).
- [30] D.D. Ryutov *et al.* Astrophys. J. **518**, 821 (1999).
- [31] P. Hartigan *et al.*, Astrophys. J. , **414**, L121 (1993).

FIG. 1: Schematic of the experimental setup, focal spot (measured) and target geometry. The laser energy distribution is modeled by means of a hybrid phase plate (HPP) resulting in a central disc and an outer ring. The nested target fits this geometry, consisting in a central iron (Fe $15\mu\text{m}$) disc and an outer plastic (CH $15\mu\text{m}$) ring on a common CH-Al pusher. The laser hits the front side of the target and the plasma emanates from the rear..

FIG. 2: Typical time resolved rear side self-emission data for a) the iron disc only and b) the complete nested target.

FIG. 3: X-ray radiography of the iron flows from a) the central disk alone, where the outer ring was blocked on the laser side and b)-h) from the complete nested target. In this case, the temporal evolution shows the formation of a collimated flow being stable up to very long delays (80 ns) and reaching mm sizes. In the insertion at 100 ns we have enhanced the contrast.

FIG. 4: Upper panel: simulated density (upper) and pressure (lower) maps at different time delays. Lower panel: corresponding synthetic radiographs obtained using the simulated density map and the experimental X-ray spectrum.

FIG. 5: Streamlines on density and pressure maps for simulations at 8 ns (a) and 20 ns (b) showing the “focusing” of the iron on the axis as it strikes the shock. The transmitted shock in Fe, the reflected shock in CH and the contact discontinuity in-between are clearly distinguishable in the density map at 20 ns. Color scheme is same as in Fig. 4

TABLE 1: Parameter values for the experiment and typical astrophysical cases on scales where collimation occurs. The index j stands for “jet” while the index a for “ambient”, represented in the experiment by the Fe and CH respectively. V is the velocity, c_s the sound velocity, l the longitudinal length, r the radial extension, ρ the density, t_{rad} is the cooling time, while t_{hydro} is the hydrodynamic one. χ is the thermal diffusivity, calculated as in [30]. c is the speed of light

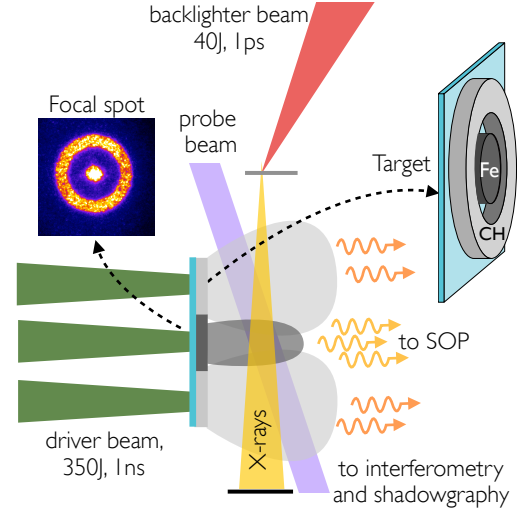


FIG. 1: Schematic of the experimental setup, focal spot (measured) and target geometry. The laser energy distribution is modeled with a hybrid phase plate (HPP) resulting in a central disc and an outer ring. The nested target fits this geometry, consisting in a central iron (Fe $15\mu\text{m}$) disc and an outer plastic (CH $15\mu\text{m}$) ring on a common CH-Al pusher.

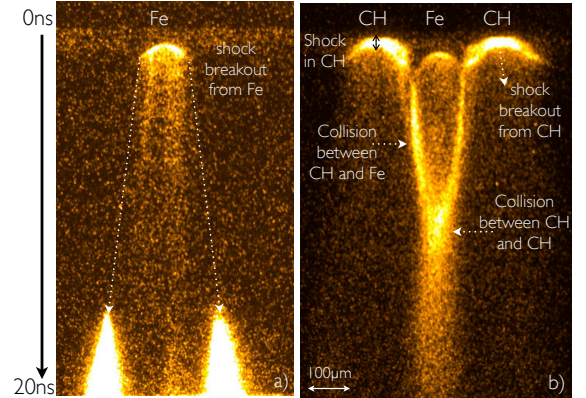


FIG. 2: Typical time resolved rear side self-emission data for a) the iron disc only and b) the complete nested target.

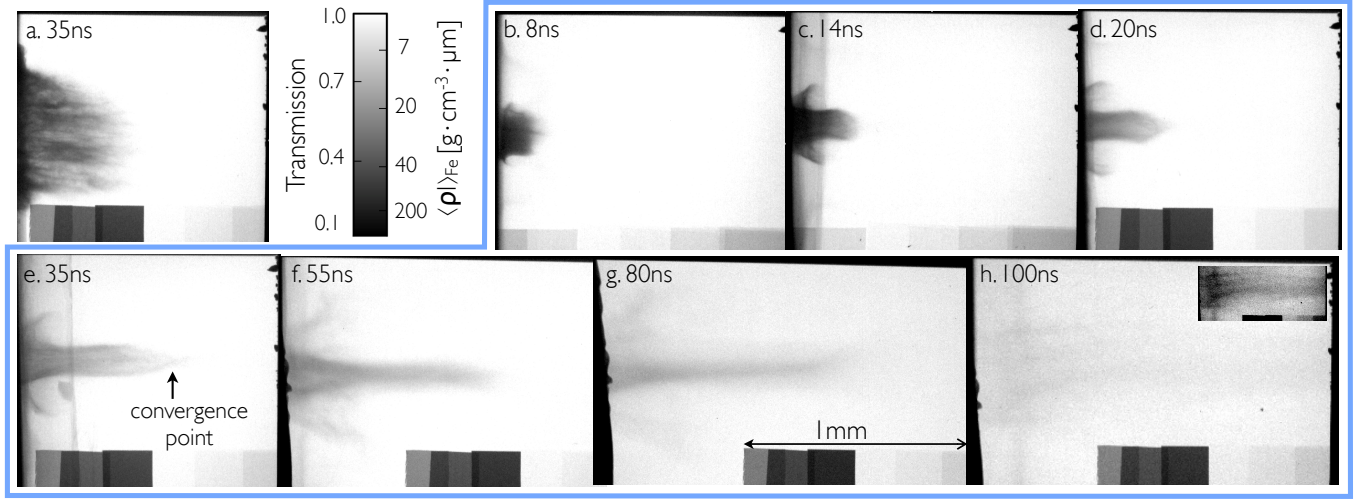


FIG. 3: X-ray radiography of the iron flows from a) the central disk alone, where the outer ring was blocked on the laser side and b)-h) from the complete nested target. In this case, we see the formation of a collimated flow being stable up to very long delays (80 ns) and reaching mm sizes. In the insertion at 100 ns we have enhanced the contrast.

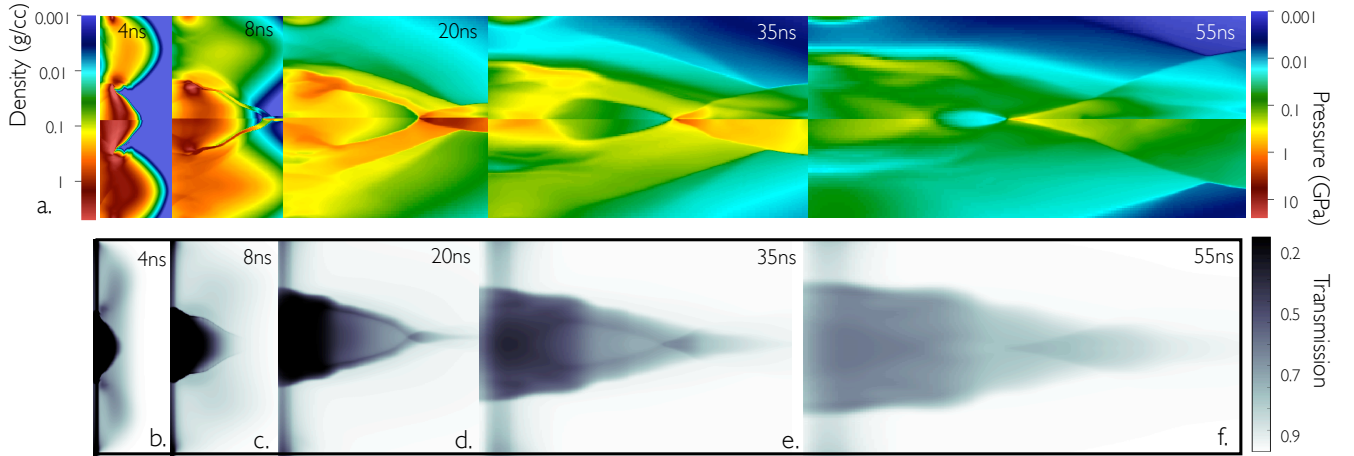


FIG. 4: Upper panel: simulated density (upper) and pressure (lower) maps at different time delays. Lower panel: corresponding synthetic radiographs obtained using the simulated density map and the experimental X-ray spectrum.

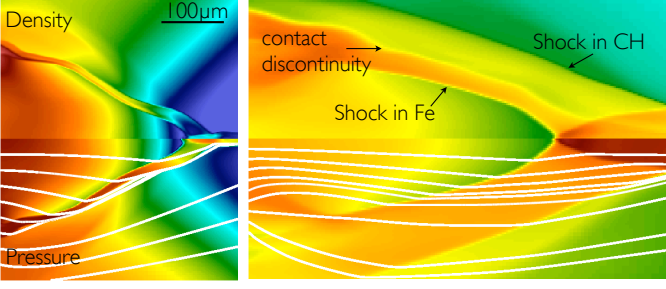


FIG. 5: Streamlines on density and pressure maps for simulations at 8 ns (a) and 20 ns (b) showing the “focusing” of the iron on the axis as it strikes the shock. The transmitted shock in Fe, the reflected shock in CH and the contact discontinuity in-between are clearly distinguishable in the density map at 20 ns. Color scheme is same as in Fig. 4

TABLE I: Experimental vs. astrophysical parameters on scales where collimation occurs. The indices j and a refer to “jet” and “ambient”, represented in the experiment by the Fe and CH respectively. V is velocity, c_s is sound speed, l is the longitudinal length, r the radial extension, ρ the density, t_{rad} is the cooling time, t_{hydro} is the hydrodynamic time. χ is the thermal diffusivity, as in [30]. c is the speed of light

| Parameter | Lab. | YSO | PPN | AGN |
|--------------------------------------|-----------|-------------|------------|----------|
| collimation scale | 1mm | $10^{-3}pc$ | $< 0.01pc$ | 0.1pc |
| Int. Mach $M_{int}=V_j/c_{s,j}$ | 5-10 | > 10 | > 10 | > 10 |
| Ext. Mach $M_{ext}=V_j/c_{s,a}$ | 5-10 | > 10 | > 10 | > 10 |
| aspect ratio $AR = l_j/r_j$ | 5 | 10 | 10 | > 10 |
| density ratio $\eta = \rho_j/\rho_a$ | 5-10 | 10 | < 1 | $<< 1$ |
| Cooling $\chi = t_{rad}/t_{hydro}$ | 100 | < 1 | < 1 | $>> 1$ |
| Peclet $Pe = \rho r V_j / \chi$ | 10^4 | $>> 1$ | $>> 1$ | $>> 1$ |
| $\beta = V_j/c$ | 10^{-4} | 10^{-3} | 10^{-3} | 0.9-0.99 |